Energy & Environmental Science

Cite this: *Energy Environ. Sci.*, 2011, **4**, 4124

www.rsc.org/ees

PAPER

Multiscale molecular simulations of the nanoscale morphologies of P3HT:PCBM blends for bulk heterojunction organic photovoltaic cells†

Cheng-Kuang Lee, Chun-Wei Pao* and Chih-Wei Chu

Received 20th April 2011, Accepted 11th July 2011
DOI: 10.1039/c1ee01508g

In this study, we developed a multiscale molecular simulation framework including coarse-grained (CG) molecular simulation, reverse-mapping, and morphology evaluation schemes to investigate the nanoscale morphologies of bulk heterojunction (BHJ) blend films comprising poly(3-hexylthiophene) (P3HT) and the methanofullerene derivative PCBM. A stable and phase-separated blend film with the fibrillar P3HT structure was observed after CG simulation of the thermal annealing process, and by the reverse-mapping technique the atomistic details—showing strong π–π interaction between thiophene rings—were retrieved. To evaluate the morphologies of P3HT:PCBM blends, a spatial-discretization scheme was developed. With such a scheme, we estimated the average domain sizes, interface-to-volume ratios, and percolation ratios of the blends at different P3HT:PCBM weight ratios. The average domain sizes determined through these simulations were in excellent agreement with those reported experimentally. Moreover, our simulations indicated that blend films having weight ratios close to 1 : 1 would have the highest interface-to-volume ratio and the most balanced charge carrier transport in both the P3HT and PCBM phases, consistent with the experimental observation that a 1 : 1 weight ratio is optimal for P3HT:PCBM blends. The multiscale molecular simulation framework proposed herein can be extended to investigating the morphologies of other photoactive layers of organic photovoltaic cells.

1. Introduction

Bulk heterojunction (BHJ) organic photovoltaic cells[1–12] are promising candidates for the future production of renewable energy because of their low production cost, high mechanical flexibility, and light-weight.[3,11,13,14] At present, the photovoltaic power conversion efficiencies of BHJ cells can reach 5%,[3,8,11] with a highest reported value of 7.6%.[9] The BHJ layer comprises two different materials: electron donors and electron acceptors. The electron donor materials are usually semiconducting conjugated polymers [*e.g.*, regioregular poly(3-hexylthiophene) (P3HT)] (Fig. 1); the electron acceptor materials [*e.g.*, [6,6]-phenyl-C_{61}-butyric acid methyl ester (PCBM)] (Fig. 1) usually exhibit strong

Research Center for Applied Sciences, Academia Sinica, 128 Sec. 2 Academia Rd., Taipei, 11529, Taiwan. E-mail: cwpao@gate.sinica.edu.tw
† Electronic supplementary information (ESI) available. See DOI: 10.1039/c1ee01508g

Broader context

Bulk heterojunction (BHJ) organic photovoltaic cells are promising renewable energy sources because of their low production cost, high mechanical flexibility, and light-weight. The BHJ layer featuring a nanoscale interpenetrating network of electron donor/acceptor phases is critical for the overall device performance. Hence, characterization of the structure of the BHJ layer is crucial for connecting various processing conditions with resultant device performance; however, this is never a trivial task from an experimental perspective. In this manuscript, we employed multiscale molecular simulations to study morphologies of the P3HT:PCBM blend during thermal annealing. From multiscale molecular simulations, we can study systems with sizes compatible with experiments, and extract morphological properties that are difficult to extract from experiments; furthermore, by reverse-mapping the atomistic details can be retrieved to study atomic packing and transport properties. By analyzing blend morphologies, we demonstrate that thermal annealing can substantially improve the crystallinity of P3HT, and the optimal blend ratio 1 : 1 for the P3HT:PCBM blend can be attributed to its highest interface-to-volume ratio, and most balanced charge transport among all blending ratios investigated. Hence, this article provides a multiscale molecular simulation framework which can be extended to any BHJ systems to help researchers characterize and design BHJ cells with superior efficiency.

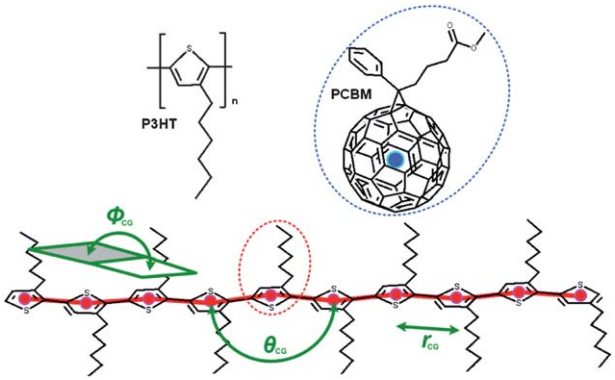

Fig. 1 Chemical structures of P3HT and PCBM. Pink beads designate the CG representation of P3HT monomers; a blue bead designates the CG representation of a PCBM molecule. The intramolecular degrees of freedom between the CG particles of P3HT monomers are highlighted.

electron affinity.[1–8,10,15,16] When incident photons are absorbed by the electron donor materials, excitons (electron/hole pairs) are generated; these electron/hole pairs are normally bound together at room temperature;[17] the mobile excitons diffuse and dissociate—that is, form free electrons and holes—at the electron donor–electron acceptor interface. Subsequent transport and collection of the photoinduced charges at the cathode and anode generate the photovoltaic current. Therefore, the key features leading to high photovoltaic conversion efficiency in BHJ photovoltaic cells are efficient separation of electron/hole pairs and prevention of charge recombination.[18] These requirements can be met in the BHJ layer by forming an interpenetrating network of electron donor/acceptor domains that maximize the interfacial area, maintain domain sizes compatible with the exciton diffusion length (*ca.* 10 nm in P3HT),[8] and ensure percolation to facilitate charge transfer. Therefore, there are three relevant morphological quantities that influence the performance of BHJ cells:

(1) The domain size of the electron donor phase must be sufficiently small so that excitons can diffuse to the electron donor–electron acceptor interface.

(2) The interface-to-volume ratio of the blend must be large to ensure efficient exciton dissociation.

(3) The percolation ratio (*i.e.*, the volume fraction of electron donor and acceptor phases that percolates through the blend) must be high to ensure charge carrier transport and collection at both electrodes to generate photocurrents.

Thus, the nanoscale morphology of the photoactive layer is a critical factor influencing the performance of BHJ cells[1–12] and a deep understanding of the effects that various processing conditions (*e.g.*, electron donor/acceptor weight ratios) have on the resultant morphologies of the BHJ layer will be important if we are to fabricate BHJ cells with superior performance.

Although the nanoscale morphology of the BHJ layer has a very important effect on the overall device performance, experimental characterization of the three-dimensional microstructure of the BHJ layer is not trivial. Morphological characterizations of BHJ layers have mostly relied on transmission electron microscopy (TEM)[1] and atomic force microscopy (AFM),[19] even though they can provide only two-dimensional images. Hence, the morphology of the blend can be characterized only for those regions close to the electrodes; the detailed structure within the BHJ layer is not revealed. Several techniques have been developed recently to provide insight into the bulk structures of BHJ layers: confocal microscopy to probe exciton lifetime,[20] cross-sectional TEM,[15] and electron tomography, which are capable of reconstructing three-dimensional structures through a series of TEM projections.[4,21] These new techniques can provide valuable information regarding the structure across the entire thickness of the blend film. Nevertheless, of the three important morphological quantities mentioned above, these new characterization tools can estimate only the average domain size;[15,20,22] determining the interface-to-volume and percolation ratios remains beyond the capability of present experimental techniques.

Multiscale modelling has been applied to studying gas adsorption of nanoporous materials with energy applications.[36] In the present study, for the first time, multiscale modelling is employed to investigate the morphological properties of BHJ organic photovoltaic cells. We developed a multiscale molecular simulation framework including CG molecular simulations based on atomistic molecular simulations (AMD),[24–34] reverse-mapping techniques,[24,26,32] and morphology evaluation schemes to investigate the nanoscale morphology of P3HT:PCBM blends. We performed a series of CG molecular simulations to investigate the formation of interpenetrating networks of P3HT:PCBM blends of various weight ratios during thermal annealing. We obtained stable and phase-separated blends with fibrillar structures in the P3HT domains, consistent with experimental observations;[1–8] furthermore, through the reverse-mapping technique, we could retrieve the atomistic configuration of the blend,[24,26,32] and could identify strong π–π packing among P3HT chains from the radial distribution function (RDF). We developed a spatial-discretization scheme to allow comprehensive analysis of the average domain size d, the interface-to-volume ratio γ, and the percolation ratio ρ. The average domain sizes determined from our CG simulation are in excellent agreement with those determined experimentally[1,15,22] and are compatible with the typical exciton diffusion length; furthermore, we found that a P3HT:PCBM weight ratio of 1 : 1 provided the highest interface-to-volume ratio and the most-balanced electron and hole transport. This multiscale simulation framework, therefore, provides insight into the optimal weight ratios of P3HT:PCBM blends based on quantitative analysis of their nanoscale morphologies. Furthermore, it can readily be used to characterize the relevant morphological features of blends of other electron donor/acceptor materials, feeds parameters computed from CGMD for more coarse-grained models such as Ising model simulations,[35] or provides morphologies required for transport calculations.[23] Thus, the present manuscript provides a multiscale molecular simulation framework that can be used to perform annealing simulations and subsequent morphology analysis, potentially assisting the development of BHJ devices exhibiting superior performance.

2. Models and methods

Fig. 1 displays the chemical structures of P3HT and PCBM. To build the CG model, each P3HT repeat unit was coarse-grained into a CG bead centered at the mass center of the individual unit

it represented (pink beads in Fig. 1); the PCBM molecule was also coarse-grained into a single bead (blue bead in Fig. 1). Using such CG model, it is possible to simulate the effects of polydispersity by introducing P3HT chains with given chain length distribution, or simulate the effects of regioregularity by introducing "defective" P3HT CG beads.[32] We employed a structure-based CG scheme to fit the force field between CG particles.[24–34] In this CG scheme, the CG force field is fitted to reproduce structural properties (*e.g.* RDF, bond length, angle, and dihedral distribution) of CG degrees of freedom computed from all-atom AMD simulations of the system of interest (with smaller size). It must be noted that the level of coarse-graining employed in the present study is good for investigating the mesoscopic properties of P3HT:PCBM blend (*i.e.* domain sizes, shapes, interface-to-volume ratio, *etc.*). To get atomistic scale details such as atomic packing, reverse-mapping procedures must be carried out, and we will describe the reverse-mapping scheme we employed in the present study at the end of this section.

Intramolecular interactions

To obtain force field parameters describing the intramolecular interactions between CG particles within P3HT molecules (*i.e.*, interactions between neighboring pink beads in Fig. 1), the trajectories of the AMD simulation of a system comprising an isolated 10-mer P3HT chain were analyzed to compute the distributions of the CG particle bond length r, bond angle θ, and planar angle ϕ. The AMD simulations were performed using DL_POLY_2 and DL_POLY_4 MD simulation packages[37,38] and incorporated DREIDING force fields.[39] The Nosé–Hoover NVT ensemble (423 K) and periodic boundary condition were employed with a time step of 1 fs and a cutoff distance of 15 Å for all non-bonding interactions. To ensure that the data collected for the atomistic model accurately described the equilibrium distributions of r and θ, the initial chain conformations for the original atomistic model were created with a Monte Carlo scheme[40] and subsequently equilibrated with an AMD simulation for 10 ns; then, after Jacobian corrections, the distributions of r, θ, and ϕ were employed to construct the underlying CG potential functions by using the Boltzmann inversion

$$U(z) = -k_{\mathrm{B}}T\ln\, P(z), \tag{1}$$

where k_{B} is the Boltzmann constant, T is the absolute temperature, and $P(z)$ is the probability distribution function of the independent variable z (*i.e.*, r, θ, or ϕ) defined in the CG polymer model. The obtained potential functions were fitted into analytic forms (Table 1) using the simplex optimization to determine the optimal parameter values. For the simplex optimizations of the intramolecular potentials, the penalty function

$$f = \int_0^{\mathrm{cutoff}} \left(U^{\mathrm{AMD}}(z) - U_i^{\mathrm{CGMD}}(z,\{p_n\})\right)^2 \mathrm{d}z \tag{2}$$

was minimized with respect to the full set of parameters, $\{p_n\}$, for the equilibrium CG bond force constant and lengths $\{k_{\mathrm{b}},r_0\}$, the bond bending force constant and angles $\{k_\theta,\theta_0\}$, and the dihedral constants $\{V_1,V_2,V_3\}$, respectively. The analytical forms and model parameters are compiled in Table 1. To ensure the reliability of the current CG model, we performed a separate CG-model-based MD simulation (CGMD), and compared the distribution functions of the CG bond lengths, angles, and planar angles from the CGMD simulation with those from the AMD simulation. Fig. S1 (ESI†) reveals that the distribution functions from the CGMD simulation fit those from the AMD simulation very well, guaranteeing that the chain conformations and associated structural features would be captured well in subsequent CGMD simulations.

Intermolecular interactions

To construct the intermolecular potential for non-bonded beads in the CG model, the radial distribution functions (RDFs) $G(r)$ from AMD simulations of particle bath systems (*i.e.*, systems comprising P3HT and PCBM monomers) were computed (see Fig. S2 in the ESI†). An iterative procedure was adopted to find

Table 1 Potential functions and parameters used for the CG models of the polymer and fullerene derivative

	Intra-/intermolecular potentials	Notation	Parameters
Bond	$U_{\mathrm{bond}} = \frac{1}{2}k_{\mathrm{b}}(r_{ij}-r_0)^2$	k_{b}: force constant, r_0: equilibrium bond length	$k_{\mathrm{b}} = 216.19$ kcal mol^{-1} Å^{-2}, $r_0 =$ 3.82 Å
Bond angle	$U_{\mathrm{angle}} = \frac{1}{2}k_\theta(\theta_{jik}-\theta_0)^2$	k_θ: force constant, θ_0: equilibrium bond angle	$k_\theta = 130.25$ kcal mol^{-1} rad^{-2}, $\theta_0 =$ 2.65 rad
Dihedral angle	$U_{\mathrm{dihed}} = \frac{1}{2}V_1(1+\cos\phi)+\frac{1}{2}V_2(1-\cos 2\phi)+\frac{1}{2}V_3(1+\cos 3\phi)$	V_1, V_2, V_3: constants	$V_1 = 0.56$ kcal mol^{-1}, $V_2 = -1.08$ kcal mol^{-1}, $V_3 = 0.28$ kcal mol^{-1}
van der Waals	$U_{\mathrm{vdw}} = 4\varepsilon\left[(\sigma/r_{ij})^{12}-(\sigma/r_{ij})^{6}\right]$	ε, σ: van der Waals parameters	$\varepsilon_{\mathrm{P3HT-P3HT}} = 0.26$ kcal mol^{-1}, $\sigma_{\mathrm{P3HT-P3HT}} = 4.95$ Å, $\varepsilon_{\mathrm{PCBM-PCBM}} = 1.61$ kcal mol^{-1}, $\sigma_{\mathrm{PCBM-PCBM}} = 9.35$ Å, $\varepsilon_{\mathrm{P3HT-PCBM}} = 0.45$ kcal mol^{-1}, $\sigma_{\mathrm{P3HT-PCBM}} = 7.15$ Å

the effective pair-potential in the Lennard-Jones form using the Boltzmann inversion as the first guess:

$$U_{i=1}^{\mathrm{CGMD}}(r) = 4\varepsilon[(\sigma/r)^{12} - (\sigma/r)^{6}] \approx -k_{\mathrm{B}}T\ln\left(\mathrm{RDF}^{\mathrm{AMD}}(r)\right) \quad (3)$$

For the simplex optimizations of the intermolecular potentials, the penalty function

$$f = \int_{0}^{\mathrm{cutoff}} \left(\mathrm{RDF}^{\mathrm{AMD}}(r) - \mathrm{RDF}_{i}^{\mathrm{CGMD}}(r, U_{i}^{\mathrm{CGMD}}\{p_n\})\right)^2 \mathrm{d}r \quad (4)$$

was minimized with respect to the full set of Lennard-Jones parameters $\{p_n\}$ and the corresponding CG intermolecular potential function of the i^{th} iteration, $U_i^{\mathrm{CGMD}}\{p_n\}$. In this present study, there were only two parameters in $\{p_n\}$, namely the potential well depth ε and the equilibrium bond length σ of the Lennard-Jones potential. In subsequent iterations, $\mathrm{RDF}_i^{\mathrm{CGMD}}$ was obtained by running CGMD simulation for 10 ns and then simplex optimization provided suggestions for the values of (σ,ε) to be used in the next CGMD simulation. With this iteration scheme, good agreement between the RDFs from CGMD and AMD simulations could be reached for each case with the bath containing single or mixed particle species (see the solid lines in Fig. S2 of the ESI†). The Lennard-Jones parameters fitted through simplex optimization are listed in Table 1.

Reverse-mapping procedure

In order to retrieve atomistic details from configurations generated from CGMD, the following procedure was employed:

(1) Prepare equilibrium atomistic structures of a P3HT monomer and a PCBM molecule.

(2) Replace the CG model with the atomistic structures.

(3) Rotate a P3HT monomer or PCBM molecule as a trial move.

(4) Determine if the trial move is accepted by using the Metropolis Monte Carlo algorithm.

(5) Repeat steps 3 and 4 until the whole system relaxes.

(6) Run MD simulation again to relax the whole system from back-mapping.

In the CGMD simulations of thermal annealing of P3HT:PCBM blends, the *NPT* ensemble using the Nosé–Hoover thermostat and barostat with coupling constants of 0.1 ps and 1 ps, respectively, was employed. The system temperature and pressure were set at 423 K and 1 atm; all the boundaries were periodic; the time step was 10 fs for CGMD simulations; DL_POLY_2 and DL_POLY_4 simulation packages were employed. A typical simulation of 40 ns simulation time of the system shown in Fig. 3 ($\sim 33 \times 33 \times 33$ nm^3) took approximately 500 hours on a 12-core server. The persistence length of P3HT computed from the CG force field fitted is 3.3 nm, which is in excellent agreement with experimental measurements.[41] In the next section, we will demonstrate that the domain size and shape computed from our CGMD simulations are in excellent agreement with those from experiments, which implies that the CGMD model developed in the present study is adequate for understanding BHJ characteristics. Note that in the present CG model of the BHJ layer we did not take the effects of electrodes into account. Hence, in this study, we investigate the bulk of the BHJ layer. We will discuss the effects of electrodes on BHJ morphology in our future publication.

3. Results and discussions

We started with a smaller system with a thinner simulation cell along the z direction (simulation cell dimensions were 33.16, 33.16, and 3.16 nm along the x, y, and z directions, respectively), because it was easier to visualize the nanoscale structural evolution of the blend (along the z direction). Fig. 2a–c display time sequence snapshots of a P3HT:PCBM blend (molecular weight of P3HT: 16 800) annealed at 423 K, determined from our coarse-grained molecular dynamics (CGMD) simulations; only the P3HT molecules are displayed (red strips) for clarity. At the beginning of the annealing process, all of the P3HT (and PCBM) molecules were oriented randomly (Fig. 2a); after 0.1 ns, the onset of phase separation occurred, with the P3HT molecules beginning to repel the PCBM molecules and crystallize (Fig. 2b); finally, after 10.0 ns, fibrillar P3HT crystals were evident (left half of Fig. 2c). Bright-field TEM,[1] electron tomography,[4] and energy-filtered TEM[22] experiments reveal fibrillar P3HT crystals in phase-separated BHJ films; hence, our CGMD simulation is in excellent agreement with experiments. The P3HT/PCBM domains were well-separated and stable (see below). When we performed a separate CGMD simulation of the same system at 300 K, no noticeable phase separation occurred on the time scale of our CGMD simulations. Thus, the phase separation at 300 K was much slower than that at 423 K.

Due to the smoother potential surface of the CG force field from coarse-graining, in CGMD simulations the barriers are in general lower; hence, the dynamics of the CGMD simulation is "accelerated" compared with all-atom MD.[33] Therefore, the CGMD time displayed at the bottom of Fig. 2a–c does not correspond to those of all-atom MD. One can get insights into the time-scaling between CGMD and the underlying atomistic MD by comparing the P3HT end-to-end correlation time between CGMD and all-atom MD simulations. A time-scaling factor of 15.6 is obtained. Therefore, the CGMD simulation time scale of the system shown in Fig. 2 is approximately of the order of 10^{-1} μs.

In order to gain insights into the atomistic details and packing of the blend, we reverse-mapped the CG particles back to atomistic configurations. The left half of Fig. 2c presents images of the P3HT:PCBM blend after 10.0 ns (*cf.* right half of Fig. 2c) in the CG representation and in the atomistic representation after proper relaxation. In the atomistic representation, we computed the radial distribution function (RDF) of each thiophene ring of the P3HT molecules at $t = 0.0$ (Fig. 2a), 0.1 (Fig. 2b), and 10.0 ns (Fig. 2c), see Fig. 2d. In Fig. 2d, it is clear to see the development of three peaks at values of r of 3.9, 5.2, and 8.1 Å during the annealing process—corresponding to the interactions A, B, and C, displayed schematically in Fig. 2d, respectively, and indicating strong π–π interactions. Note that when computing RDFs, we excluded the contributions from thiophene rings on the same P3HT chain. In electron diffraction experiments of P3HT:PCBM blends (and pure P3HT), a strong (020) reflection is often observed—indicating π–π stacking between P3HT chains.[4,21,22] Thus, the combination of CG modeling and reverse mapping allowed us to successfully

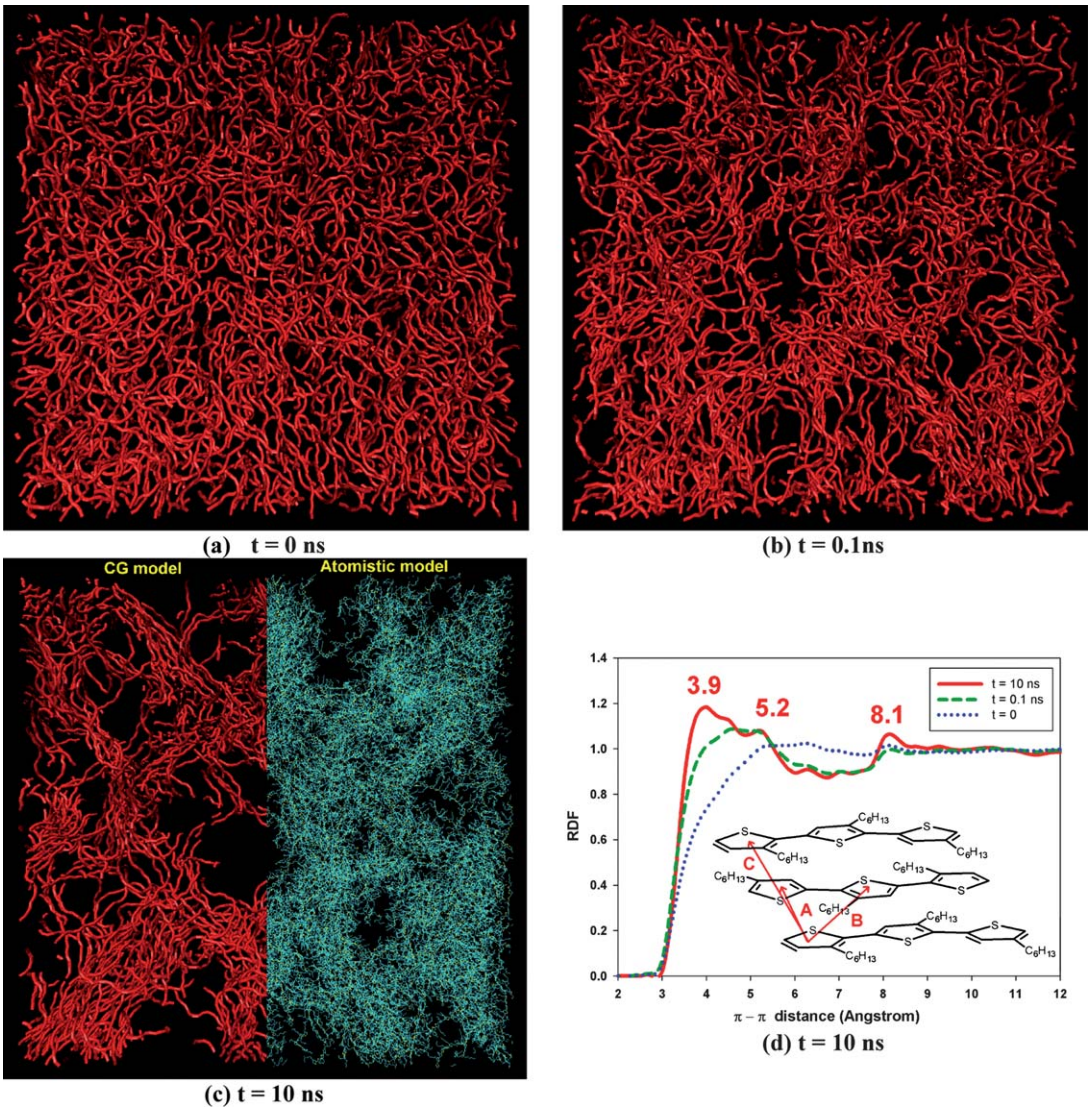

Fig. 2 (a–c) Time sequence snapshots of the P3HT:PCBM blend film at a weight ratio of 1 : 1, from CGMD simulations at $T = 423$ K; (c) the system after reverse-maps back to atomistic representation (right) and the CG representation (left). (d) RDF of thiophene rings after reverse mapping; three possible interactions between thiophene rings (A–C) are represented schematically. In (a)–(c), only P3HT molecules are shown for clarity.

reproduce the experimentally observed P3HT crystallization and π–π stacking between P3HT molecules. With atomistic representations, a specific region in the whole blend can be further investigated using first-principles calculations to explore relevant electronic transport properties; this feature is, however, beyond the scope of this paper.

Nanoscale morphologies at different P3HT:PCBM weight ratios

To characterize the morphological properties (*i.e.*, average domain sizes, interface-to-volume ratios, percolation ratios) of the bulk of P3HT:PCBM blends, we performed CGMD annealing simulations on a larger system (the dimensions of the simulation cell were now *ca.* 30 nm along the *X*, *Y*, and *Z* directions; see Fig. 3). To understand the effect of the P3HT:PCBM weight ratio on the resultant morphologies of the blends, we performed CGMD simulations at P3HT:PCBM weight ratios of 2 : 1, 1 : 1, 1 : 2, and 1 : 3. Because we imposed constant pressure (1 atm) boundary conditions in this study, the simulation cells were different for all of the investigated weight ratios. Fig. 3 reveals that phase separation occurred for each of the weight ratios. In the case of the 2 : 1 (1 : 2 and 1 : 3) weight ratio, the P3HT (PCBM) phase occupied most of the simulation cell; in the case of the 1 : 1 weight ratio, an interpenetrating network appeared to form between the two phases, with a morphology resembling the "column-like" structures from both cross-sectional and energy-filtered TEM.[15,22,42] Nevertheless, a method for quantifying all of the relevant morphological quantities would be necessary to understand the effects of the different weight ratios on the nanoscale morphologies and, consequently, the efficiencies of BHJ cells.

Morphological characterization

We developed a spatial-discretization scheme to analyze the relevant morphological quantities of the photoactive layer. In

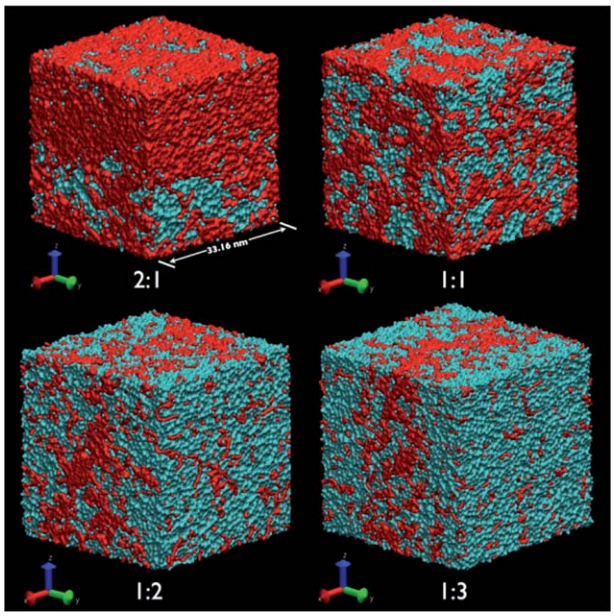

Fig. 3 Morphologies of blends with P3HT:PCBM weight ratios of (a) 2 : 1, (b) 1 : 1, (c) 1 : 2, and (d) 1 : 3. Simulations were performed at 423 K and 1 atm, with a simulation time of 30 ns. P3HT domains are colored in red; PCBM domains, in blue.

this scheme, we divided the entire simulation cell into equal-sized cubes (or "pixels") having dimensions (1 nm) close to those of a PCBM CG particle (Fig. 4b). To decide whether a cube belonged to either the P3HT or PCBM domain, we defined the quantity

$$\lambda = (N_{\mathrm{P3HT}}/N_{\mathrm{PCBM}})(\sigma_{\mathrm{P3HT}}/\sigma_{\mathrm{PCBM}})^3, \quad (5)$$

where N_{P3HT} and N_{PCBM} are the number of CG particles of the P3HT monomers and PCBM molecules, respectively, inside the cube and σ_{P3HT} and σ_{PCBM} are the CG particle sizes of the P3HT monomers and PCBM molecules, respectively. If λ was greater than 1.0, the cube belonged to the P3HT domain and was marked in red; otherwise, it belonged to the PCBM domain and was marked in blue, see Fig. 4b. With such a spatial-discretization scheme at hand, we could now estimate the microstructural and morphological quantities.

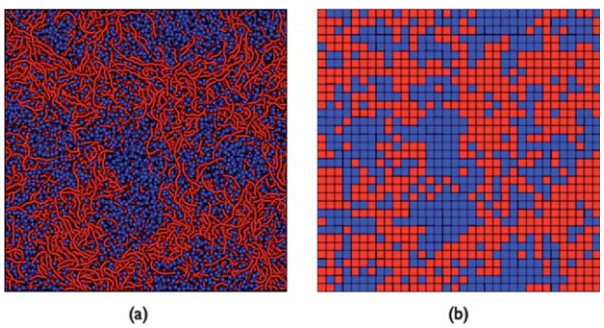

Fig. 4 Characterization of morphological properties through a spatial-discretization scheme: (a) before and (b) after spatial-discretization. P3HT molecules and domains are colored red; PCBM molecules and domains, blue.

The total area of the interface between the P3HT and PCBM phases can be estimated using the equation

$$A_{\mathrm{total}} = \sum a_{\mathrm{P3HT-PCBM}}, \quad (6)$$

where $a_{\mathrm{P3HT-PCBM}}$ is the area of the square separating neighboring P3HT and PCBM cubes in Fig. 4b (in this case, $a_{\mathrm{P3HT-PCBM}} = 1\ \mathrm{nm}^2$). The number of domains for the P3HT and PCBM phases, M_{P3HT} and M_{PCBM}, respectively, can be computed by counting non-overlapping cubes; the average domain sizes can be estimated using the formula

$$d_{\mathrm{P3HT}} = \sqrt{A_{\mathrm{total}}/(M_{\mathrm{P3HT}}\pi)}, \quad (7)$$

and

$$d_{\mathrm{PCBM}} = \sqrt{A_{\mathrm{total}}/(M_{\mathrm{PCBM}}\pi)}. \quad (8)$$

For the blend having a weight ratio of 1 : 1, Fig. 5a displays the average domain sizes of the P3HT and PCBM phases plotted with respect to the simulation time. The average domain sizes converged after 30 ns of thermal annealing. Furthermore, the estimated average domain sizes of the P3HT and PCBM phases at 40 ns were 13.43 and 11.72 nm, respectively. The estimated P3HT domain sizes from experiments of similar P3HT:PCBM blending ratios were 15.0, 13.0, and 15.0 nm for bright-field,[1] cross-section,[15] and energy-filtered TEM,[22] respectively. Therefore, once again our results are in good agreement with experimental observations.

To determine the ratio of crystallinity (*i.e.*, the volume fraction of the P3HT phase that exhibited a crystalline phase) of the bulk blend presented in Fig. 3, we employed the orientational order parameter S that is commonly used to describe the crystallinity of liquid crystals.[43] We coarse several P3HT pixels into one sub-domain and defined the following "local" order parameter S_j of each sub-domain as

$$S_j = \frac{3}{2}\left\langle (u_{ij}n_j)^2 - \frac{1}{3}\right\rangle, \quad (9)$$

where u_{ij} is the i^{th} bond vector in the j^{th} sub-domain and n_j is the average bond vector in the j^{th} sub-domain, defined as $n_j = \langle u_{ij}\rangle$. If $0.3 \leq S_j \leq 1$, the j^{th} P3HT sub-domain was considered to be crystalline.[43] After computing values of S_j for all of the P3HT sub-domains, we could determine the probability that a specific magnitude of S_j occurred in the whole blend. The histograms plotted in Fig. 5b reveal that P3HT crystallized after thermal annealing for all of the weight ratios; furthermore, by integrating the horizontal axis (*i.e.*, the S_j axis) for values of S_j from 0.3 to 1.0, we obtained ratios of crystalline P3HT in the 2 : 1, 1 : 1, 1 : 2, and 1 : 3 blends of 0.76, 0.79, 0.77, and 0.71, respectively—consistent with experimental observations from electron tomography.[1,21] In contrast, for the 1 : 1 blend prepared without annealing, the ratio of crystalline P3HT was only 0.36; hence, thermal annealing can significantly improve the degree of crystallinity of P3HT molecules.

The electron donor–electron acceptor interface-to-volume ratio γ is an indicator of the exciton dissociation efficiency; estimating this quantity experimentally remains a technical challenge. From our CGMD simulations, the interface-to-volume ratio γ of the whole blend could be estimated using the equation

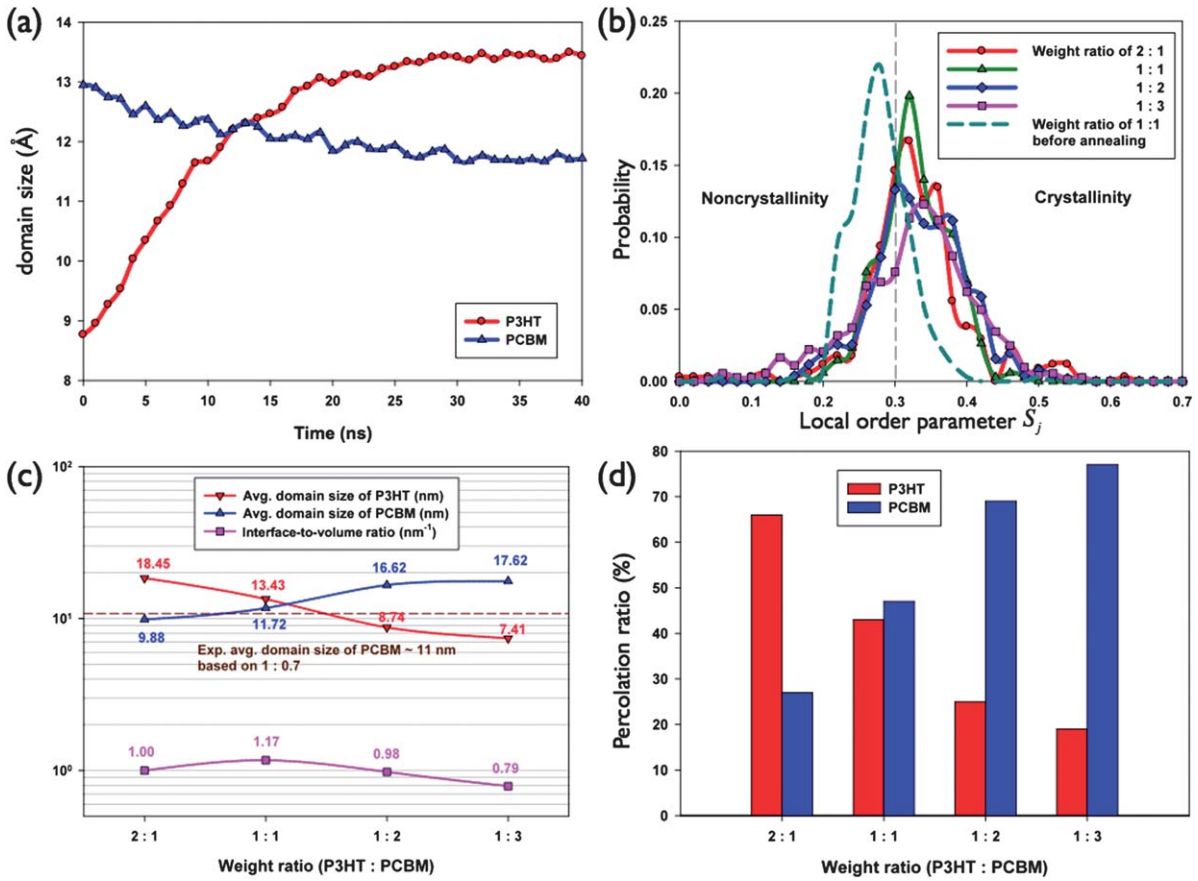

Fig. 5 Morphological properties of P3HT:PCBM blends estimated using the spatial-discretization scheme. (a) Time evolution of the average domain sizes of the P3HT and PCBM phases of the blend having a weight ratio of 1 : 1. (b) Probability distributions of the local order parameter S_j at each weight ratio. (c) Estimated average domain sizes and interface-to-volume ratios of the blends at each weight ratio. (d) Percolation ratios of the P3HT and PCBM phases at each weight ratio.

$$\gamma = A_{\text{total}}/V_{\text{box}}, \tag{10}$$

where V_{box} is the volume of the simulation cell. Fig. 5c displays the estimated interface-to-volume ratios γ and average domain sizes d for the blends at the various weight ratios. The average domain size d of the P3HT phase decreased upon increasing the PCBM weight ratio; at a P3HT:PCBM weight ratio of 1 : 1, the average domain sizes of the two phases were approximately equal. Furthermore, the interface-to-volume ratio γ reached its maximum value at a weight ratio of 1 : 1; implying that this particular P3HT:PCBM blend would exhibit optimal exciton dissociation at the P3HT–PCBM interface.

After dissociation of excitons at the donor–acceptor interface, the generated electrons (holes) must be transported to the cathode (anode). If there are any isolated electron donor (acceptor) domains (*i.e.*, cul-de-sacs), the holes (electrons) generated within such domains would be blocked and could never be transported to the cathode (anode). Thus, in addition to the interface-to-volume ratio (a morphological quantity related to the exciton dissociation rate), we wished to compute the percolation ratios ρ for both the P3HT and PCBM phases to quantify the volume fraction of each phase that the charge carriers could percolate through the simulation cell. With the periodic boundary conditions employed in this study, we employed the following algorithm to compute the percolation ratio ρ:

(1) Divide the simulation cell into N slices along the Z direction of the simulation cell.

(2) Pick one slice (i) and select one P3HT (PCBM) pixel (j) on this slice.

(3) Test whether we could start from pixel j, find a continuous pathway across the periodic boundary, and reach slice i from the other side.

(4) Repeat this process for all of the P3HT (PCBM) pixels on slice i, and compute the fraction ρ_i of P3HT (PCBM) pixels at slice i that could percolate through the cell.

(5) Repeat steps (2)–(4); the percolation ratio ρ of the P3HT (PCBM) phase can then be computed as

$$\rho = \frac{1}{N}\sum_i \rho_i$$

Fig. 5d displays the percolation ratios ρ of both the P3HT and PCBM phases at each of the weight ratios investigated in this study. In the case of the 2 : 1 weight ratio, the percolation ratio of the P3HT phase was substantially higher than that of the PCBM phase, implying there were many isolated PCBM domains. At

a weight ratio of 1 : 1, the percolation ratios of both the P3HT and PCBM phases were approximately equal. Not surprisingly, upon increasing the PCBM weight ratio, the P3HT percolation ratios underwent significant declines. From the perspective of charge carrier transport, the electrons and holes generated at the donor–acceptor interface in the blend having a weight ratio of 1 : 1 had almost the same probabilities of being collected by their respective electrodes, thereby generating a photocurrent; in contrast, for the blend featuring a 2 : 1 (1 : 3) weight ratio, despite higher hole (electron) conductivity, most of the electrons (holes) generated would be trapped within isolated PCBM (P3HT) domains. Hence, from the perspective of the nanoscale morphology of the P3HT:PCBM blend, the optimal electron donor/acceptor weight ratio (1 : 1) resulted from the highest interface-to-volume ratio (for efficient exciton dissociation) and from the most-balanced percolation ratios between the electron donor/electron acceptor phases (preventing generated charges from becoming trapped within isolated domains).

Using the characterization tools and simulation methodologies developed in this study, it would be straightforward to construct CG models for other electron donor/electron acceptor materials. From these CG models, a series of CGMD annealing simulations can be performed to compute the average domain sizes, interface-to-volume ratios, and percolation ratios; these morphological insights would characterize the nanoscale morphologies of the blends and allow optimal weight ratios to be determined. Furthermore, reverse mapping makes it possible to retrieve atomistic configurations, which can be used in subsequent quantum transport calculations to determine electronic transport properties.

4. Conclusion

We have performed a series of CGMD simulations to investigate the thermal annealing processes of P3HT:PCBM blends at various weight ratios. We constructed a CG model based on knowledge from all-atom molecular dynamics simulations and employed a spatial-discretization scheme to quantify several morphological quantities related to BHJ cell efficiency: namely, the domain sizes (for exciton diffusion), the interface-to-volume ratio (for exciton dissociation at the donor–acceptor interface), and the percolation ratios of both the donor and acceptor phases (for subsequent charge carrier transport to electrodes). Through such an analysis, we conclude that the optimal weight ratio of 1 : 1 of P3HT:PCBM blend can be attributed to its largest interface-to-volume ratio and most balanced charge carrier transport. This approach provides valuable insight into the nanoscale morphologies, which are difficult to measure experimentally, of P3HT:PCBM and other BHJ systems; furthermore, the multiscale molecular simulation framework developed in this study can be used to investigate the morphologies of other BHJ materials, potentially aiding the development of more-efficient organic photovoltaic devices.

Acknowledgements

We thank for the Research Center for Applied Science, Academia Sinica, and the National Science Council of Taiwan (project no. NSC 99-2112-M-001-004-MY3) for financial support. We also thank for Prof. Chun-Wei Chen, National Taiwan University and Prof. Julia W.P. Hsu, University of Texas at Dallas, for insightful discussions.

Notes and references

1 X. Yang, J. Loos, S. Veenstra, W. J. H. Verhees, M. M. Wienk, J. M. Kroon, M. A. J. Michels and R. A. J. Janssen, *Nano Lett.*, 2005, **5**, 579.
2 E. Klimov, W. Li, X. Yang, G. G. Hoffmann and J. Loos, *Macromolecules*, 2006, **39**, 4493.
3 G. Dennler, M. C. Scharber and C. J. Brabec, *Adv. Mater.*, 2009, **21**, 1323.
4 S. van Bavel, E. Sourty, G. de With, K. Frolic and J. Loos, *Macromolecules*, 2009, **42**, 7396.
5 A. M. Ballantyne, T. A. M. Ferenczi, M. Campoy-Quiles, T. M. Clarke, A. Maurano, K. H. Wong, W. Zhang, N. Stingelin-Stutzmann, J. S. Kim, D. D. C. Bradley, J. R. Durrant, I. McCulloch, M. Heeney and J. Nelson, *Macromolecules*, 2010, **43**, 1169.
6 G. Li, Y. Yao, H. Yang, V. Shrotriya, G. Yang and Y. Yang, *Adv. Funct. Mater.*, 2007, **17**, 1636.
7 Z. Xu, L. M. Chen, G. Yang, C. H. Huang, J. Hou, Y. Wu, G. Li, C. S. Hsu and Y. Yang, *Adv. Funct. Mater.*, 2009, **19**, 1227.
8 L. M. Chen, Z. Hong, G. Li and Y. Yang, *Adv. Mater.*, 2009, **21**, 1434.
9 H. Y. Chen, J. Hou, S. Zhang, Y. Liang, G. Yang, Y. Yang, L. Yu, Y. Wu and G. Li, *Nat. Photonics*, 2009, **3**, 649.
10 A. Kumar, R. Devine, C. Mayberry, B. Lei, G. Li and Y. Yang, *Adv. Funct. Mater.*, 2010, **20**, 2729.
11 B. Kippelen and J.-L. Brédas, *Energy Environ. Sci.*, 2009, **2**, 251.
12 H. Borchert, *Energy Environ. Sci.*, 2010, **3**, 1682.
13 C. J. Brabec, N. S. Sariciftci and J. C. Hummelen, *Adv. Funct. Mater.*, 2001, **11**, 15.
14 A. C. Mayer, S. R. Scully, B. E. Hardin, M. W. Rowell and M. D. McGehee, *Mater. Today*, 2007, **10**, 28.
15 J. S. Moon, J. K. Lee, S. Cho, J. Byun and A. J. Heeger, *Nano Lett.*, 2009, **9**, 230.
16 B. Watts, W. J. Belcher, L. Thomsen, H. Ade and P. C. Dastoor, *Macromolecules*, 2009, **42**, 8392.
17 M. Pope and C. E. Swenberg, *Electronic Processes in Organic Crystals and Polymer*, Oxford University Press, Oxford, 1999.
18 J. Guo, H. Ohkita, H. Benten and S. Ito, *J. Am. Chem. Soc.*, 2010, **132**, 6154–6164.
19 W. Ma, C. Yang, X. Gong, K. Lee and A. J. Heeger, *Adv. Funct. Mater.*, 2005, **15**, 1617–1622.
20 J. Huang, F. Chien, P. Chen, K. Ho and C. Chu, *Anal. Chem.*, 2010, **82**, 1669–1673.
21 S. van Bavel, E. Sourty, G. de With and J. Loos, *Nano Lett.*, 2008, **9**, 507.
22 L. F. Drummy, R. J. Davis, D. L. Moore, M. Durstock, R. A. Vaia and J. W. P. Hsu, *Chem. Mater.*, 2011, **23**, 907.
23 J. A. Anta, *Energy Environ. Sci.*, 2009, **2**, 387.
24 W. Tschöp, K. Kremer, J. Batoulis, T. Bürger and O. Hahn, *Acta Polym.*, 1998, **49**, 61.
25 D. Reith, H. Meyer and F. Müller-Plathe, *Macromolecules*, 2001, **34**, 2335.
26 F. Müller-Plathe, *ChemPhysChem*, 2002, **3**, 754.
27 H. Fukunaga, J. I. Takimoto and M. Doi, *J. Chem. Phys.*, 2002, **116**, 8183.
28 R. Faller and D. Reith, *Macromolecules*, 2003, **36**, 5406.
29 E. S. Boek, J. T. Padding, W. K. den Otter and W. J. Briels, *J. Phys. Chem. B*, 2005, **109**, 19851.
30 P. Carbone, F. Negri and F. Müller-Plathe, *Macromolecules*, 2007, **40**, 7044.
31 W. G. Noid, J. W. Chu, G. S. Ayton, V. Krishna, S. Izvekov, G. A. Voth, A. Das and H. C. Andersen, *J. Chem. Phys.*, 2008, **128**, 244114.
32 C. K. Lee, C. C. Hua and S. A. Chen, *Macromolecules*, 2011, **44**, 320–324.
33 P. Carbone, H. A. K. Varzaneh, X. Chen and F. Müller-Plathe, *J. Chem. Phys.*, 2008, **128**, 064904.
34 C. Peter and K. Kremer, *Soft Matter*, 2009, **5**, 4357.
35 B. Lei, Y. Yao, A. Kumar, Y. Yang and V. Ozolins, *J. Appl. Phys.*, 2008, **104**, 024504.

36 Z. Xiang, D. Cao, J. Lan, W. Wang and D. P. Broom, *Energy Environ. Sci.*, 2010, **3**, 1469.
37 W. Smith and T. R. Forester, *The DL_POLY_2 Reference Manual*, Laboratory Daresbury, Daresbury, 2001.
38 I. T. Todorov and W. Smith, *The DL_POLY_4 Reference Manual*, Laboratory Daresbury, Daresbury, 2010.
39 S. L. Mayo, B. D. Olafson and W. A. Goddard, *J. Phys. Chem.*, 1990, **94**, 8897.
40 D. P. Landau and K. Binder, *A Guide to Monte Carlo Simulations in Statistical Physics*, Cambridge University Press, New York, 2001.
41 B. Cesar, M. Rawiso, A. Mathis and B. François, *Synth. Met.*, 1997, **84**, 241.
42 J. W. Kiel, B. J. Kirby, C. F. Majkrzak, B. B. Maranville and M. E. Mackay, *Soft Matter*, 2010, **6**, 641.
43 P. J. Collings and M. Hird, *Introduction to Liquid Crystals*, Taylor & Francis, Bristol, 1997.

